JOURNAL OF MATERIALS SCIENCE **40** (2005) 6483–6494

An investigation of the effect of high-temperature cyclic straining and creep loading on tensile mechanical properties of GH4145/SQ alloy

DUYI YE, ZHENLIN WANG
Department of Mechanics, Zhejiang University,, Hangzhou 310027, People's Republic of China
E-mail: duyi_ye@zju.edu.cn

XIAOXIA YIN
Huaxin P&T Consulting and Designing Institute Co., Ltd.,, Hangzhou 310006, People's Republic of China

Published online: 5 October 2005

The effect of the reverse cyclic straining and the creep loading on the resultant tensile mechanical properties, such as the strength parameter ($\sigma_{0.2}$ and σ_b), the ductile parameter (δ and φ_f) and the composite parameter of the strength and ductility, the static toughness (U_t), for the precipitation-strengthened nickel-based superalloy GH4145/SQ used for high-temperature turbine and valve studs/bolts in power plant was investigated systematically at a temperature of 538°C. The experimental results show that in the case of the reverse cyclic straining both $\sigma_{0.2}$ and σ_b increases at early stages of cyclic straining and, after reaching their saturated values, $\sigma_{0.2}$ remains relatively constant until about 90% of fatigue life, while σ_b exhibits continuous reduction up to a level equal to the maximum applied stress amplitude. With the increasing number of straining cycles, both δ and φ_f as well as U_t decrease significantly until final fracture. In the case of creep loading the strength parameters ($\sigma_{0.2}$ and σ_b) tend to increase, as a whole, while the ductile parameters (δ and φ_f) and the static toughness (U_t) exhibit continuous decrease characterization as the amount of the creep deformation increases. The variation of the aforementioned various tensile mechanical properties during cyclic straining and creep loading of the alloy was further discussed by means of the observations of the deformation microstructures as well as the examinations of the fracture features of the specimens.

1. Introduction

Mechanical properties of a material in monotonic loading, such as the strength, ductility and static toughness, provide the most fundamental information for material-evaluation in strength analysis and lifetime prediction of structural components and elements. It has been indicated that these material properties not only depend on various metallurgical factors, such as grain size, alloying element, quenching, aging, and annealing, etc., but are intensively influenced by service conditions including loading history, state of stress imposed, environment, temperature, etc. [1]. High-temperature mechanical loading, such as reverse cyclic straining, creep loading, etc., can introduce significant changes in microstructure of crystalline materials, such as: (1) nucleation, growth and migration of new phases; (2) dimensional and morphological changes, migration and disappearance of old phases; (3) grain-boundary sliding and migration; (4) formation of subgrains; (5) changes of dislocation density, configuration and distribution; (6) nucleation, growth and coalescence of grain-boundary voids; (7) migration of undesirable elements to grain boundaries [2, 3]. Some of the aforementioned microstructural changes may result in a notable deterioration in mechanical properties of materials, such as reduction in the tensile strength, ductility, fracture toughness, etc. [4–6]. This deterioration in mechanical properties involves a complex interaction among material, mechanical loading and environment. When the deterioration of the material mechanical properties reaches its critical value below which the material loses its load-bearing capacity, a dangerous situation may arise for structures and components operating in elevated-temperature service conditions. It is therefore suggested that the safety life of materials which serve while loaded at high temperatures should be determined by their resultant mechanical properties rather than by their initial values.

0022-2461
DOI: 10.1007/s10853-005-1548-0

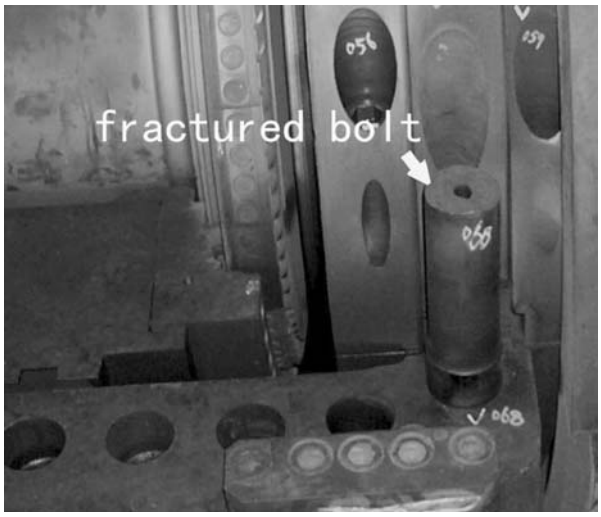

Figure 1 Photograph of a fractured bolt in high-pressure turbine inner cylinder.

GH4145/SQ is a precipitation-strengthened nickel-based superalloy with good high temperature strength and oxidation resistance. This alloy is currently used for the fabrication of high-temperature turbine and valve studs/bolts in high (middle)-pressure cylinders of high capacity steam turbines in power plant. In such applications it is usually subjected to creep loading due to tensile stress resulting from tightening by thermal and mechanical means in the studs/bolts and fatigue loading due to start-stop operation and power fluctuations during turbine running. The failure of the high-temperature turbine and valve studs/bolts mostly results from the interaction of creep and low-cycle fatigue (LCF) in their practical service conditions [7, 8]. As an example, Fig. 1 shows a photograph of a broken high-pressure inner cylinder stud. Therefore, it is of important practical significance to investigate the effect of high-temperature cyclic straining and creep loading on the tensile mechanical properties of GH4145/SQ superalloy, such as the strength, ductility and static toughness, and accordingly to provide a basis for the establishment of remaining lifetime prediction methods for turbine and valve studs/bolts operating in high-temperature where creep deformation exists and where cyclic conditions prevail. In this paper we reported experimental results on this aspect. The variation of the various tensile mechanical properties during LCF and creep loading of the alloy was further discussed by means of examinations of deformation microstructures and fracture features of the specimens.

2. Material and experimental procedures

The material used in this study was precipitation-strengthened nickel-based alloy GH4145/SQ, which was received as rod that had been hot forged to 30 mm in diameter. The alloy composition in percentage weight is shown in Table I. The rods were solution treated at 1135°C for 8 h followed by air-cooled and then aged at 835°C for 24 h and at 695°C for 20 h and finally they were air-cooled to room temperature. Segments cut from the heat-treated rods were prepared for machining low-cycle fatigue-type specimens with a gauge length of 14 mm and gauge diameter of 6 mm and creep-type specimens with a gauge length of 50 mm and gauge diameter of 10 mm, respectively. Prior to testing, all specimens were first mechanically polished with abrasive papers and then lapped with alumina powders.

Experiments for the current study comprised, (1) constant amplitude low-cycle fatigue tests to produce specimens with various pre-cyclic deformation, (2) constant-stress creep tests to produce specimens with various creep deformation, (3) both tensile-after-cyclic-loading tests and tensile-after-creep-loading tests to determine the resultant tensile mechanical properties, (4) optical and transmission-electron microscopy observations of fatigued and crept specimens to investigate the deformation microstructures, and (4) scanning electron microscope examinations on the tensile fracture surfaces to determine the predominant fracture modes.

2.1. Constant amplitude low-cycle fatigue tests

Fully reversed, push-pull, total axial strain controlled low-cycle fatigue tests, with the aid of elevated-temperature longitudinal extensometer of 12 mm gauge length, were performed at a temperature of 538°C on a computer-controlled 100 kN MTS 809 closed-loop servo-hydraulic test machine inside a three-zone furnace where a temperature of ±2°C was maintained. Test temperature was measured by using three thermocouples attached to the parallel portion of a specimen and controlled for temperatures at three measured points to obtain uniform temperature. A triangular strain waveform with zero mean strain at a constant total strain rate of 4.0×10^{-3} s^{-1} was used. The strain amplitude chosen for the present investigation was 0.5% resulting in the fatigue failure life of 4669 cycles. Fatigue life in this test was defined as the cycles corresponding to a 25% drop in the maximum load. Low-cycle fatigue tests were interrupted at various chosen portions of the fatigue life fraction before fracturing. During testing, the load was continually monitored and hysteresis loops were recorded at appropriate intervals. The pre-cyclically strained specimens were then used for tensile tests at elevated temperature without reshaping.

2.2. Constant-stress creep tests

Constant-stress creep tests were performed at temperature of 538°C under a tensile stress of 500 MPa in a Schenck RMC 100 testing machine. In these tests,

TABLE I Chemical composition (wt%) of GH4145/SQ alloy

C	Mn	Si	S	P	Cr	Ni	Co	Cu	Al	Ti	Fe	Nb	Mg	Zr	B
0.08	0.35	0.35	0.01	0.015	15.0	Balance	1.0	0.5	0.60	2.5	6.0	1.0	0.01	0.06	0.002

specimens are first loaded in constant strain-rate conditions at a nominal strain-rate of nearly 6×10^{-5} s^{-1}. Then, at a given stress level, the testing machine is suddenly switched to the load-control mode and the specimens are allowed to deform under creep conditions. The test temperature was monitored with two thermocouples touching the specimen gauge section and held constant within ±2°C for each individual test. Specimen displacement was measured using a linear variable displacement transformer (LVDT) that was attached to the ridges of the creep specimen interfaced with a data acquisition system, which made it possible to measure the creep strain to within ±0.03%. In order to produce specimens with various amounts of creep deformation, creep tests were interrupted at various chosen creep times before rupture. These crept specimens were then machined into standard tensile specimens with a gauge length of 14 mm and gauge diameter of 6 mm for subsequent tensile failure tests at elevated temperature.

2.3. Uniaxial tensile failure tests

Uniaxial tensile failure tests were carried out on pre-cyclically deformed specimens and crept specimens, respectively, using the computer-controlled 100 kN MTS 809 closed-loop servo-hydraulic test machine with a strain rate of 3.0×10^{-5} s^{-1} at a temperature of 538°C. The specimens were firstly pulled to a certain strain level in a strain control mode to measure the 0.2 pct proof stress ($\sigma_{0.2}$) and then tensioned up to fracture in a displacement control mode to measure the ultimate tensile strength (σ_b), the reduction of area (φ_f) and the elongation (δ),respectively.

2.4. Microstructure observations

The microstructural changes that occurred during fatigue and creep tests were assessed by both optical microscopy (OM) and transmission-electron microscopy (TEM). Sections for microstructural analysis were prepared from the gauge portions in both pre-cyclically deformed specimens and crept specimens by cutting perpendicular to the tensile axils with a wire saw. The samples for OM were first ground using emery papers of various grinds from 230 to 600 grit and then etched for nearly 30 s in a solution of 16 g $FecCl_3$, 9 g $(NH_4)S_2O_8$, 100 ml H_2O, and 60 ml HCL at 40°C. The samples for TEM were mechanically thinned to 0.1 mm and then electro-polished in a solution containing 16 volume percentage (vol%) of perchloric acid, 4 vol% of ethanol and 80 vol% of 2-butoxyethanol using a twin jet apparatus at a potential of 20 V and a temperature below 3°C. TEM examinations were performed on a Philips CM200 transmission electron microscope.

2.5. Fracture examinations

The fracture surface of both tensile-after-cyclic-loading tested specimens and tensile-after-creep-loading tested specimens were ultrasonically cleaned in trichloroethylene and then observed using a scanning electron microscope (SEM) to determine the fine-scale features.

Figure 2 Optical micrograph showing as-heat-treated microstructure of GH4145/SQ alloy.

SEM examinations were performed with a JEOL JSM-T20 scanning electron microscopy operating at 120 kV.

3. Results and discussion

3.1. Initial tensile mechanical properties

In order to determine the effects arising from cyclic straining and creep loading, the tensile mechanical properties of the alloy in the virgin conditions had to be characterized first. Table II lists the tensile properties of virgin specimens at a temperature of 538°C. The results reported are the mean values based on multiple (three) tests. The yield strength ($\sigma_{0.2}$) and the ultimate strength (σ_b) are 598.80 MPa and 1257.0 MPa, respectively. The large difference between $\sigma_{0.2}$ and σ_b indicates that in the as heat-treatment conditions the GH4145/SQ alloy exhibits a significant amount of work hardening during monotonic deformation. The elongation to failure (δ) and the reduction of area (φ_f) are 0.24 and 0.34, respectively. These tensile mechanical properties thus reveal that the virgin alloy has high strength and medium ductility.

Optical micrograph showing the microstructure of the alloy in the heat-treatment conditions is presented in Fig. 2. Fig. 3 displays TEM micrograph for the same conditions. It is seen from Fig. 2 that the previously mentioned heat treatment produced an average equiaxed grain size of 110 μm. Both bulk and grain boundaries were covered with discrete carbide particles probably being of the MC type. Fig. 3 shows that the two-step aging employed to the alloy results in

TABLE II Tensile mechanical properties of GH4145/SQ alloy in the virgin conditions

0.2% proof stress, $\sigma_{0.2}$ (MPa)	Ultimate tensile strength, σ_b (MPa)	Elongation, δ	Reduction of area, φ_f	Static toughness, U_t (MPa)
598.80	1257.0	0.24	0.34	233.5

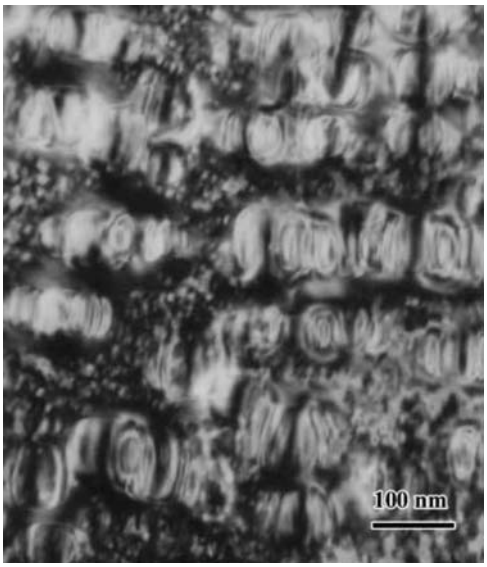

Figure 3 Bright-field transmission electron micrograph showing as-heat-treated γ' structure of GH4145/SQ alloy.

two kinds of γ' precipitate sizes. The large cuboidal γ'particles with 80 nm in size were surrounded by particles of small (approximately 20 nm) diameter. It has been indicated [9] that the size of the particles can effect the deformation mode (i.e. either shearing or looping) and hence the damage mechanisms. Small γ' particle sizes promote shearing, while larger particle sizes promote looping.

Fig. 4 shows SEM observation of the fracture surface from the tensile test of the virgin specimen. In this figure a high population of micro-voids with a wide range of sizes as well as large and deep dimples is visible on the fracture surface, indicating the highly ductile nature in the virgin, as-heat-treated alloy.

3.2. Effect of cyclic loading on tensile mechanical properties

The results of the tensile-after-cyclic-loading tests for the present alloy are reported in Table III. Fig. 5 summarizes the various tensile mechanical properties,

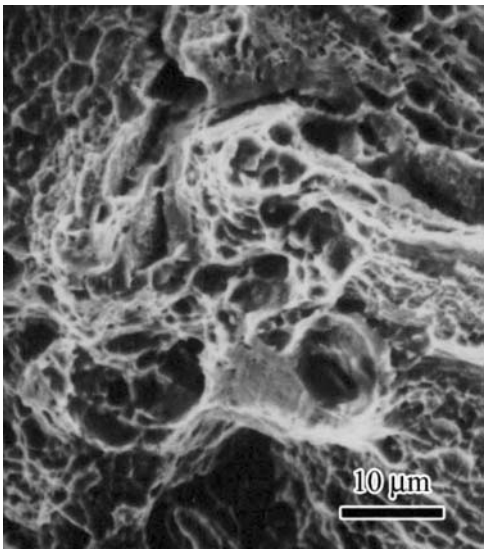

Figure 4 Fractograph of the virgin specimen.

TABLE III Typical measured data of the tensile mechanical properties of GH4145/SQ alloy at different number of straining cycles (ε_a = 0.5%)

Number of cycles (N)	$\sigma_{0.2}$ (MPa)	σ_b (MPa)	δ	φ_f	U_t (MPa)
5	625.5	1219.7	0.21	0.27	209.2
20	606.2	1227.5	0.21	0.24	217.2
100	664.4	1236.8	0.21	0.25	215.8
300	665.3	1229.6	0.22	0.27	225.7
500	668.3	1227.1	0.21	0.24	208.5
1000	684.8	1255.0	0.22	0.27	227.3
1600	668.4	1203.4	0.19	0.17	178.5
2500	667.0	958.5	0.08	0.09	60.5
3200	641.1	929.7	0.07	0.07	55.4
4000	645.5	898.3	0.07	0.08	50.2
4500	487.8	522.1	0.03	0.06	11.6

i.e. the strength parameters ($\sigma_{0.2}$ and σ_b), the ductility parameters (δ and φ_f) and the composite parameter of the strength and ductility, the static toughness (U_t) defined as the area under the stress-strain curve, as functions of the number of straining cycles, where the dashed line exhibits the tendency of the variation in the individual mechanical property parameter during high-temperature fatigue failure process. As it is seen in Fig. 5a, under the elevated-temperature reverse cyclic straining, a significant increase in $\sigma_{0.2}$ occurs during the first few cycles, and after reaching its saturated value, $\sigma_{0.2}$ remains relatively constant until about 90% of fatigue life, while a quasi-stable behavior in σ_b was observed after its slight increase at early stages of cyclic straining, and after undergoing around 2000 cycles that correspond to about 45% of the fatigue life, σ_b exhibits continuous reduction up to a level equal to the maximum applied stress amplitude. Fig. 5b shows that, with increasing number of straining cycles, both δ and φ_f decrease sharply up to final fracture. Moreover, a significant drop in these ductile parameters was observed even at very beginning of the cyclic loading. This means that the capability of the current alloy to deform plastically is sensitive to the elevated-temperature cyclic straining. The combined effect of the tensile strength and the ductility, i.e. U_t, also exhibits a continuous reduction with the number of straining cycles, as observed in Fig. 5c, indicating thereby that the applied high-temperature reverse cyclic straining dissipates the ability to absorb the deformation and fracture energy inherent in the alloy considerably.

Fig. 6 shows optical micrographs taken from a deformed region of pre-cyclically deformed specimens and fatigue fractured specimen, respectively. A corresponding TEM observation of the deformation microstructures is shown in Fig. 7. It is seen from Fig. 6 that, with increasing number of strain cycling, the degree of strain homogeneity increases, as seen by a progressive increase in the density of deformation bands and also shown by the increase in the number of grains containing deformation bands (see Figs. 6a and b). Moreover, it appears that in most of the grains only one system of parallel $\{111\}$ planes is activated. Fig. 6c indicates that the crack propagation in the cyclically deformed specimen is mainly transgranular mode. The

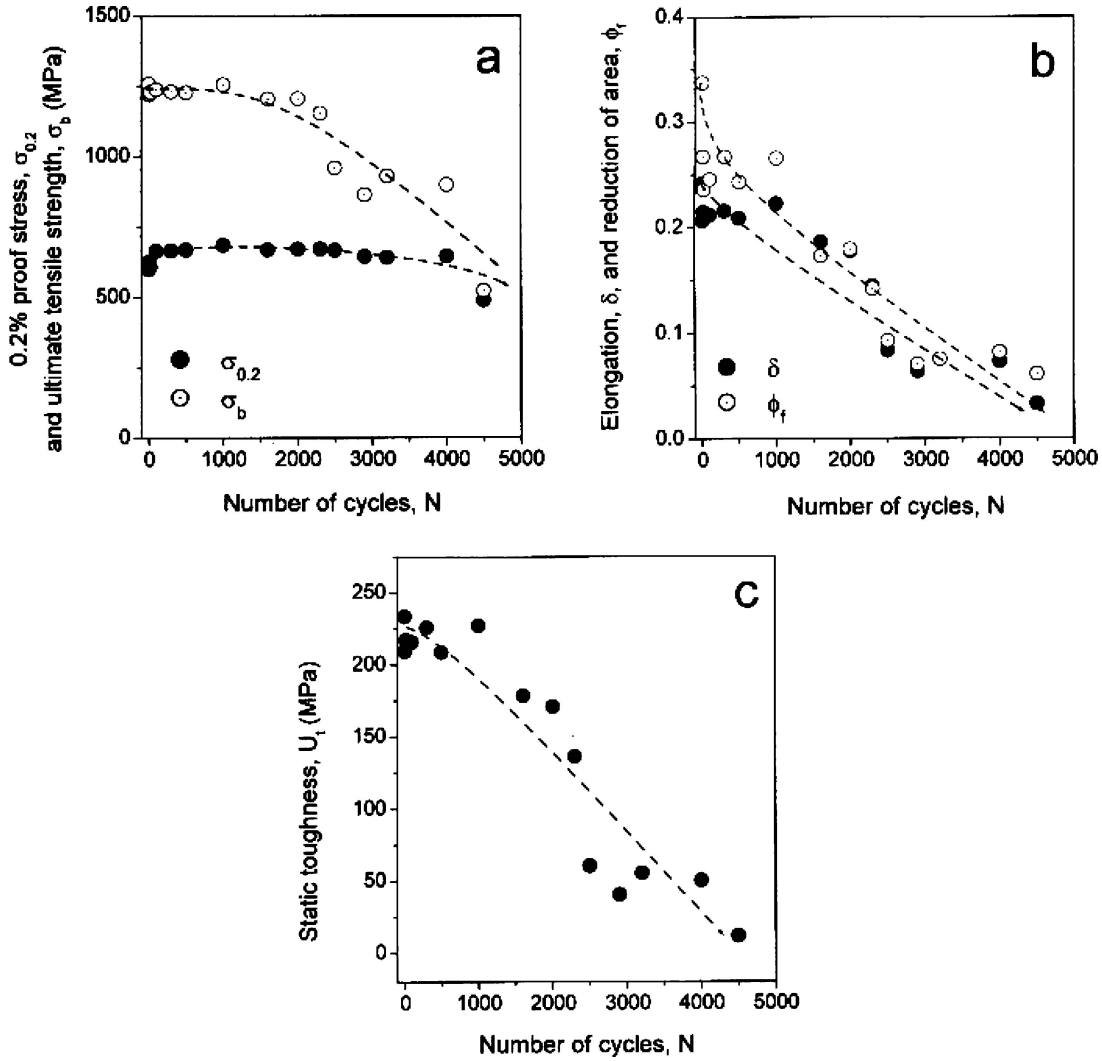

Figure 5 Variation of tensile mechanical properties during cyclic straining (a) Strength parameters ($\sigma_{0.2}$ and σ_b); (b) Ductility parameters (φ_f and δ); (c) Static toughness (U_t).

electron micrograph shown in Fig. 7a reveals that even the first 5 cycles lead to a significant increase in the dislocation density in the alloy. After undergoing 2000 straining cycles that correspond to about half-life of the specimen, the predominant deformation mode in the alloy is the precipitate shearing and bowing locally along the slip plane (Fig. 7b). The bright field micrograph shown in Fig. 7c confirms that the propagation of the deformation in the cyclically strained alloy is planar. As reported previously [10–12], in precipitation-hardened systems the resistance to plastic deformation mainly consists of two components: one due to dislocation-dislocation interaction (work hardening) and the other due to dislocation-precipitate interaction (precipitation strengthening). In the GH4145/SQ condition the original microstructures comprise a high volume fraction of strengthening precipitates and foreign particles (see Figs. 2 and 3). During cyclic straining, the mutual interactions of the dislocations and the interactions of dislocations with precipitates, grain boundaries, etc. increase the resistance to plastic deformation considerably, which may be responsible for the observed increase in the strength parameters ($\sigma_{0.2}$ and σ_b) during the early stages of strain cycling. It has also been indicated [11] that, for age-hardened nickel-based alloy, after some cumulative strain, the degradation of the original precipitates mostly took place due to dislocation-precipitate interactions. The various mechanisms suggested for precipitates degradation in precipitation-hardened systems, based on indirect evidence, are [11–15]: (1) shearing of precipitates; (2) disordering of precipitates; (3) growth of precipitates, and (4) dissolution of precipitates. In the current alloy both shearing and disordering of precipitates have been observed in the specimens after a certain number of straining cycles, whereas no evidence of growth of precipitates was found in the cyclically deformed specimens. Therefore, in accordance with the conclusion by previous investigations [13–15], the mechanisms responsible for the observed decrease characters in the strength parameters ($\sigma_{0.2}$ and σ_b) during the later stages of cyclic straining are mostly dependent on the shearing of γ' particles, which promotes softening owing to a progressive decrease in the effective precipitate cross section, the formation of γ'-free deformation bands and an early micro-crack formation in the cyclically deformed specimens.

SEM examination of fracture surfaces from the specimens subjected to various numbers of pre-straining cycles followed by monotonically tensioning to fracture is summarized in Fig. 8. As it is seen from Fig. 8a, after

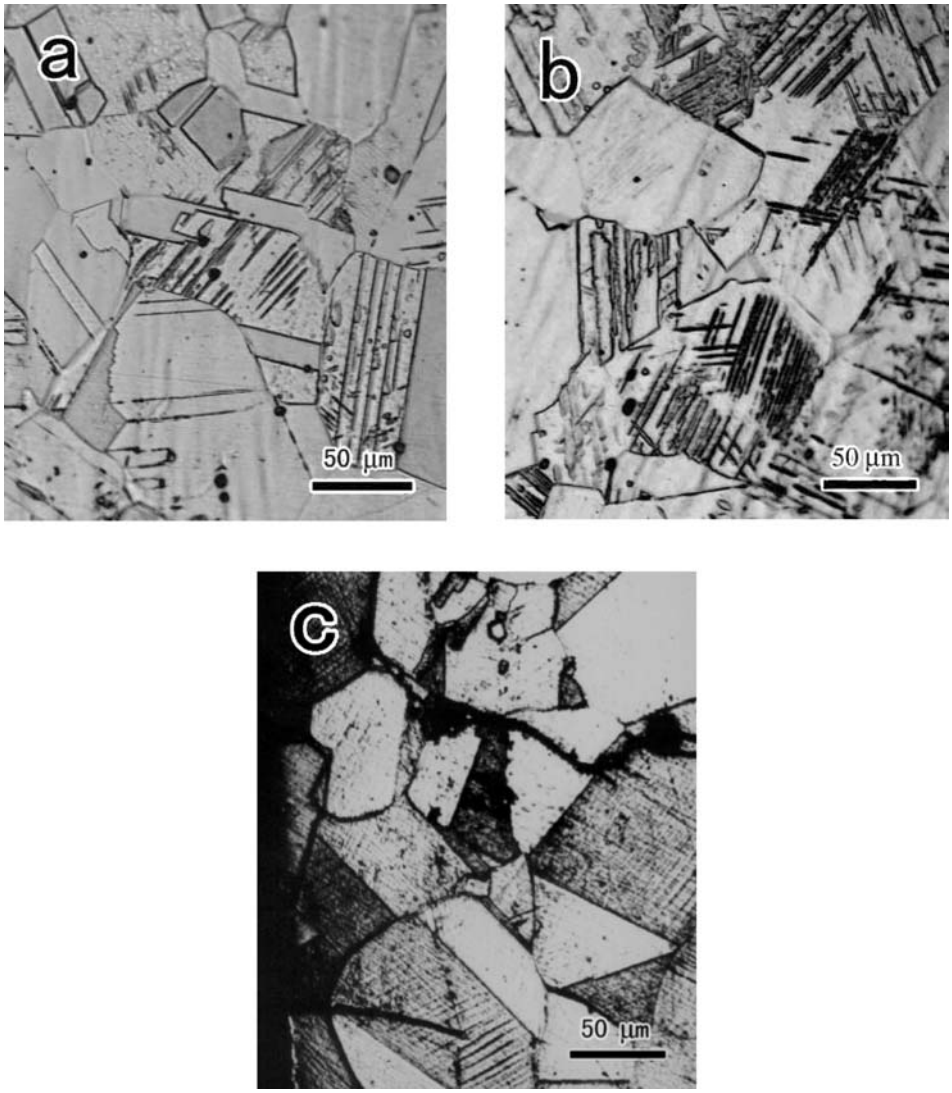

Figure 6 Optical micrographs showing slip bands in pre-cyclically deformed specimens tested at $\varepsilon_a = 0.5\%$: (a) $N = 5$ cycles; (b) $N = 500$ cycles; (c) $N_f = 4669$ cycles.

undergoing 500 straining cycles that correspond 10% of the fatigue failure life, the tensile fracture surface comprised two distinct regions, i.e. (i) a ductile region created by the growth and coalescence of voids formed with columnar grains, which exhibits similar features with those observed in the virgin specimen shown in Fig. 4, and (ii) a less ductile or apparently quasi-cleavage region created by decohesion along the grain boundaries and by coalescence of voids in the neighboring slip bands, indicating a mixed ductile/brittle fracture feature. It is evident from Fig. 8b that, by further increasing the number of straining cycles, this ductile / brittle fracture feature exhibiting on the fracture surface of the cyclically deformed specimen becomes more pronounced. The fatigued fracture surface (Fig. 8c) reveals extensive micro-cracks with a typical transgranular appearance on well-defined brittle fatigue striations. The above observation on microscopic fracture thus suggests that, with the increasing number of straining cycles, the fracture modes in GH4145/SQ alloy occurs distinct ductile-to-brittle transition (DBT), which well accords with the reduction characterization of the ductile properties (φ_f and δ) during fatigue failure process, as presented previously.

3.3. Effect of creep loading on tensile mechanical properties

The results obtained from tensile-after-creep-loading tests are summarized in Table IV. Various tensile mechanical properties ($\sigma_{0.2}$, σ_b, δ, φ_f and U_t) as functions of the creep time are shown in Fig. 9, where the dashed line shows the tendency of the variation in the individual mechanical property parameter during creep defor-

TABLE IV Typical measured data of the tensile mechanical properties of GH4145/SQ alloy at various creep times ($\sigma = 500$ MPa)

Creep time T (hours)	$\sigma_{0.2}$ (MPa)	σ_b (MPa)	δ	φ_f	U_t (MPa)
10	611.7	1231.4	0.20	0.26	211.4
50	607.2	1229.0	0.21	0.23	214.2
100	618.1	1234.7	0.20	0.22	208.8
250	620.1	1238.3	0.20	0.20	208.5
500	611.8	1245.3	0.20	0.20	210.0
1000	625.1	1252.0	0.22	0.18	195.4
2000	751.4	1281.4	0.20	0.14	175.0
2500	680.7	1276.5	0.18	0.18	167.5
3000	649.9	1274.2	0.17	0.13	200.7
3500	683.5	1286.0	0.17	0.15	180.7

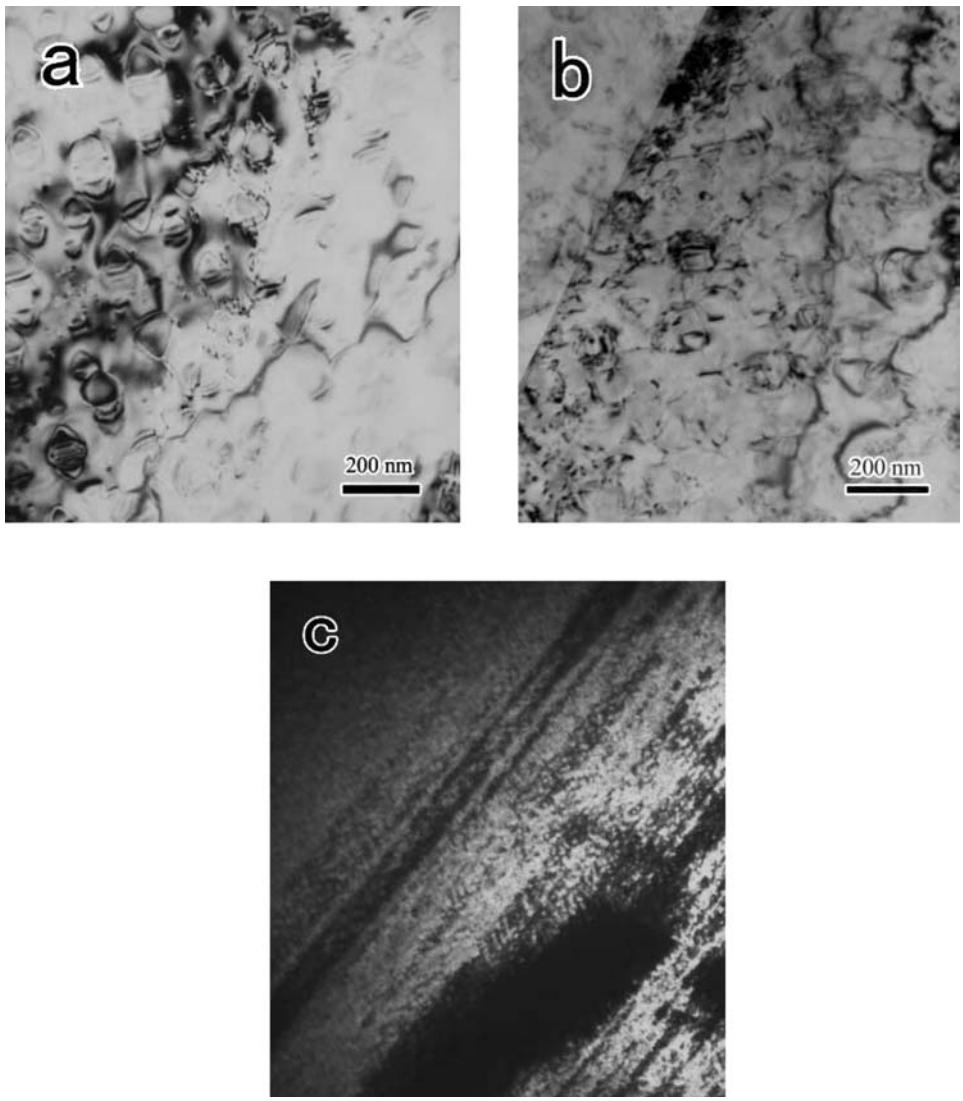

Figure 7 TEM micrographs showing distribution of dislocations in pre-cyclically deformed specimens tested at $\varepsilon_a = 0.5\%$: (a) $N = 5$ cycles; (b) and (c) $N = 500$ cycles.

mation. As it is seen in Fig. 9a, under high-temperature creep loading, both $\sigma_{0.2}$ and σ_b tend to increase, as a whole, while φ_f and δ decrease progressively with increasing creep deformation (see Fig. 9b). Moreover, a significant reduction in the ductile properties (δ and φ_f) was also observed during the early stages of the creep loading. This phenomenon is apparently as a consequence of the pre-deformation due to the initial creep loading, resulting in the decrease of the remaining plastic deformation capacity in the alloy. As the amount of the creep deformation increases, the composite property of the strength and ductility, the static toughness (U_t), also exhibits a continuous reduction characterization (Fig. 9c), indicating thereby that the applied high-temperature creep loading depletes the ability to absorb the deformation and fracture energy inherent in the alloy significantly.

The variation of the afore-presented tensile mechanical properties with the creep deformation can also be analyzed by means of the investigation of the deformation microstructure during creep loading of the alloy, which has been shown in optical micrograph in Fig. 10. As it is seen from Fig. 10a–c, under current creep loading conditions, both the morphology and the distribution of foreign particles (MC) in the alloy undergo an insignificant variation, as a whole, in comparison with those observed in the as-heat treated microstructures shown in Fig. 2. This observation can be mostly attributed to highly stable carbide particles distributed throughout the matrix and along the grain boundaries in the alloy at the present testing temperature [2]. However, in the case of the specimen crept to failure there is a significant amount of grain boundary cavitation (see Fig. 10c), and cavity linkage to give grain boundary facet cracking is clearly shown in Fig. 10d. The possible mechanisms for the formation of grain boundary cavities in the nickel-base superalloy were suggested as vacancy injection, creep due to oxide growth stresses, and gas formation [2]. It has also been indicated in previous investigations [16] that during creeping deformation of metallic materials, there is a combination of complex mechanisms that can be summarized as follows: a large amount of lattice dislocations preexist in the structure, but new dislocations are continuously created during the creep process due to the imposed load. The load makes most dislocations in grains and grain boundaries move, resulting in a lot of interactions with other components of the microstructure, such as neighboring

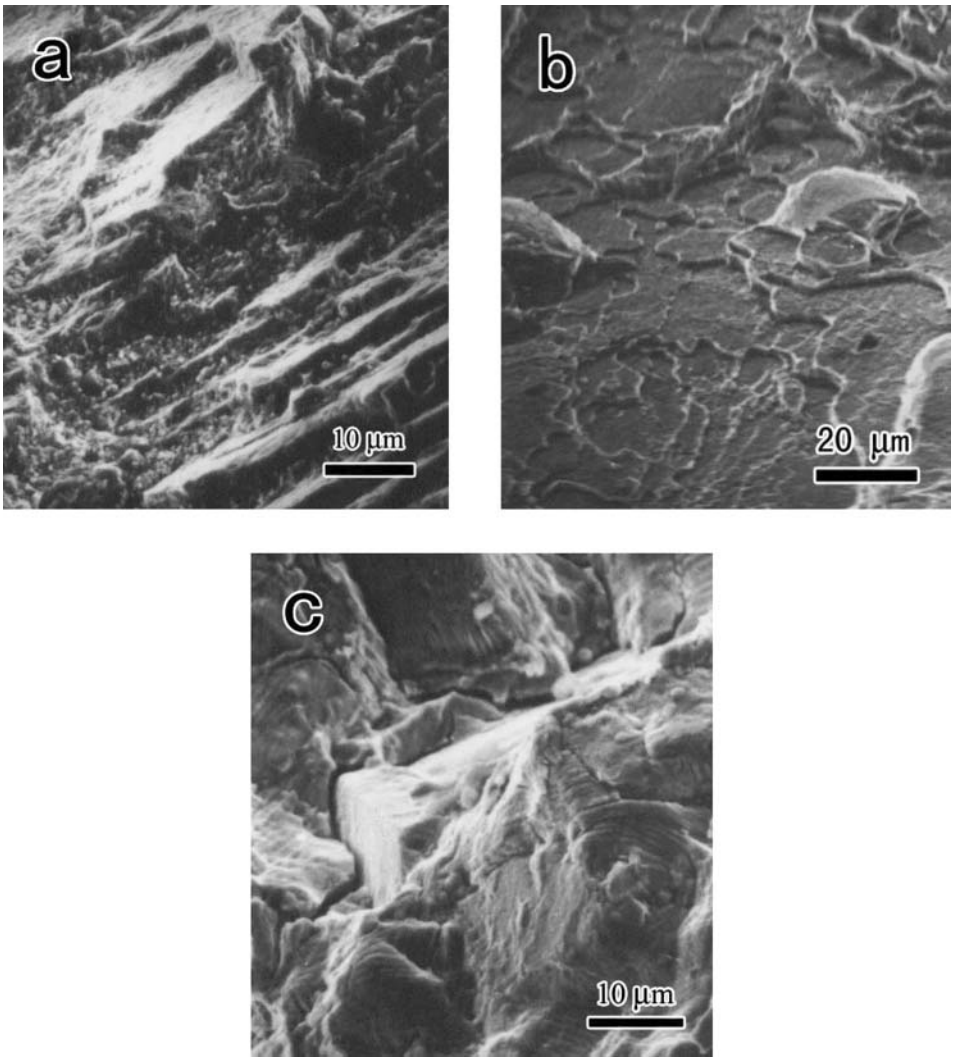

Figure 8 Fractographies of specimens pre-fatigued with different number of cycles at $\varepsilon_a = 0.5\%$ (a) $N = 500$ cycles; (b) $N = 1800$ cycles; (c) $N_f = 4669$ cycles.

dislocations, alloy atoms in solution, precipitates, dispersed phases, impurities, sub-grains, etc. Figs. 11a and b show typical TEM micrographs taken from a deformed region of the specimens subjected to creep loading for 3500 h and crept to failure, respectively. As it is seen in Fig. 11a, after a certain creep deformation, the matrix contained only large γ' particles and the original secondary distribution of fine particles has been lost during the preceding creep process. The absence of significant numbers of dislocation loops around γ' particles implies that the principle deformation mode in the present superalloy was particle cutting rather than dislocation bowing. Similar observations were also reported for other nickel-based superalloys subjected to creep loading at elevated temperature [2]. Therefore, in accordance with the micro-mechanisms mentioned above the interactions of dislocations with precipitates, grain boundaries, etc., resulting in the increase of the resistance to plastic deformation, may be responsible for the increase in the strength parameters ($\sigma_{0.2}$ and σ_b) during the creep deformation of the alloy. Since in the creep loading condition the γ' cutting mechanism does not occur so readily as in the cyclic loading condition and the deformation is much more evenly dispersed [2], this leads to a relatively small work-hardening effect in the creep loading case as compared to the cyclic loading case. It is indicated [16, 17] that under high temperature conditions the creation of dislocations in the alloy is thwarted by their annihilation due to a thermally activated restorative process. The result of the dislocation annihilation is the creation of lattice vacancies that are attracted to grain boundaries via diffusion to form micro-voids. Both vacancies and micro-voids weaken the grain boundaries, allowing the grains to slide on each other in the load direction and, as a consequence, leading to the nucleation of boundary cavities that grow and eventually link to form micro-cracks. Fig. 11b shows an observation of boundary cavities in the specimen crept to failure that were evidently associated with carbide particles as well as the vacancies and micro-voids. Thus the increased amount of grain boundary failure during creep deformation of the alloy may be responsible for the progressive decrease in ductile properties (δ and φ_f), as shown previously.

Scanning electron microscopic fractography of the specimens subjected to various creep deformation followed by monotonically tensioning to fracture is summarized in Fig. 12. This figure shows that, with the increase of creep deformation, the tension facture surface exhibits a transition feature from a ductile fracture

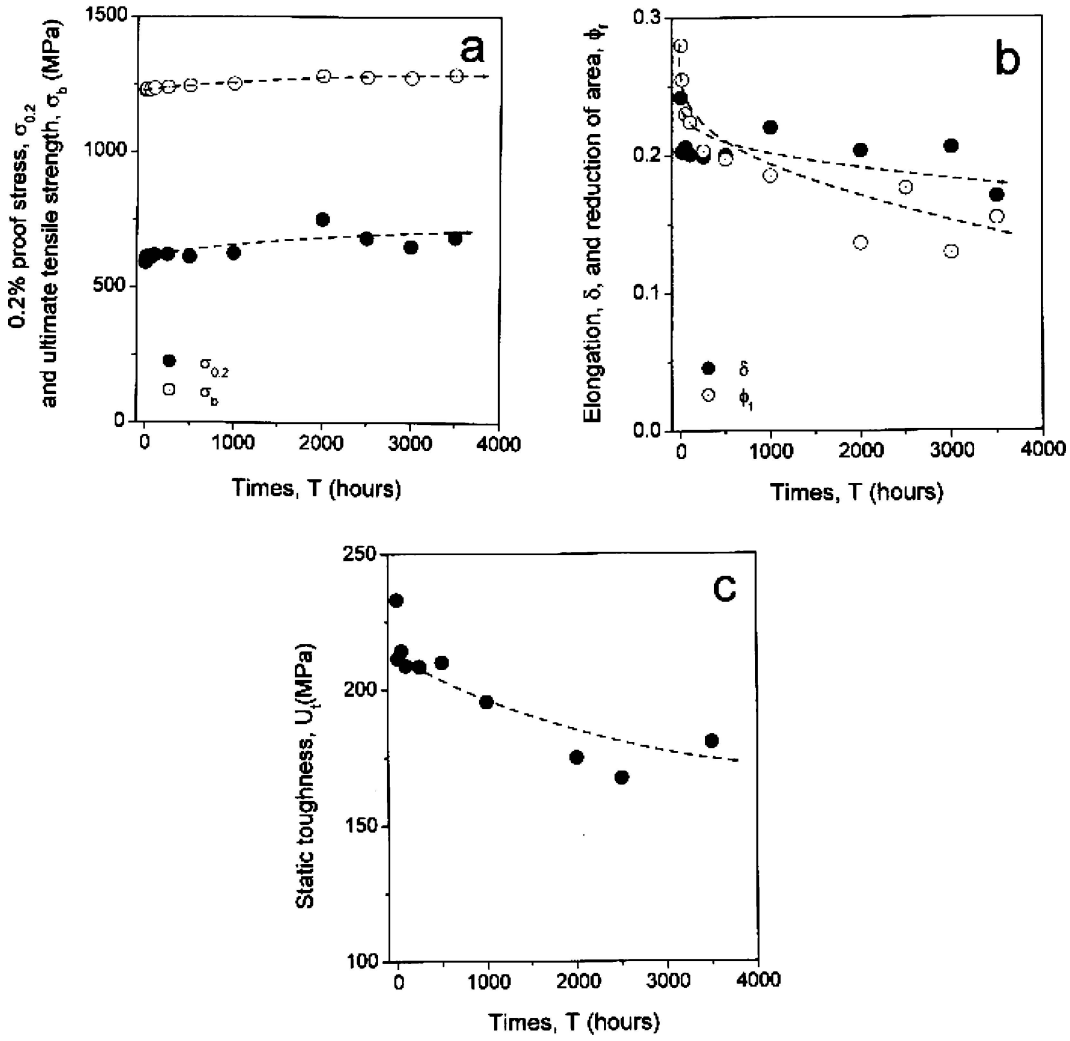

Figure 9 Variation of tensile mechanical properties during creep loading: (a) Strength parameters ($\sigma_{0.2}$ and σ_b); (b) Ductility parameters (φ_f and δ); (**c**) Static toughness (U_t).

characterized by a high population of dimples observed on most grain boundaries and grain boundary facets connected by transgranular shear surface (see Fig. 12a) to a low ductile intergranular rupture characterized by shallow dimples on the fracture surface and many voids and cracks on grain-boundary (see Figs. 7b and c). The fracture surface appearance of the creep ruptured specimen, as shown in Fig. 12d, displays the pronounced "rock candy" appearance typical for the less ductile crack growth area. As it is indicated [4], the dimpled intragranular fracture involves a considerable amount of localized plastic deformation, which in itself requires higher amounts of energy in order to fracture the specimen as compared to the amount of energy needed for intergranular fracture. This ductile-to-brittle transition (DBT) occurring on the fracture surface of the crept specimens is thus accordance with the reduction characteristics of both the ductile properties (φ_f and δ) and the static toughness (U_t) during creep failure process of the alloy.

4. Conclusions

1. The investigation regarding the effect of reverse cyclic straining on the tensile mechanical properties of nickel-based alloy GH4145/SQ at a temperature of 538°C leads to the following conclusions.

(a) Under reverse cyclic straining, the strength parameters ($\sigma_{0.2}$ and σ_b) increase at early stages of cyclic straining, and after reaching their saturated values, $\sigma_{0.2}$ remains relatively constant until about 90% of fatigue life, while σ_b exhibits continuous reduction up to a level equal to the maximum applied stress amplitude. With the increasing number of straining cycles, the ductile parameters (δ and φ_f) and the static toughness (U_t) decrease significantly until final fracture.

(b) Optical microscopic (OM) examinations show that, with increasing number of strain cycling, the degree of strain homogeneity in the alloy tends to increase and the crack propagation in the cyclically deformed specimen is mainly transgranular mode. Transmission-electron microscopic (TEM) observations reveal that, under the cyclic straining, the predominant deformation mode in the alloy is the precipitate shearing and the dislocation bowing and the propagation of the deformation in cyclically deformed specimens is planar. The change in the microstructures during cyclic straining is responsible for the variation in the static mechanical property parameters during the course of fatigue failure.

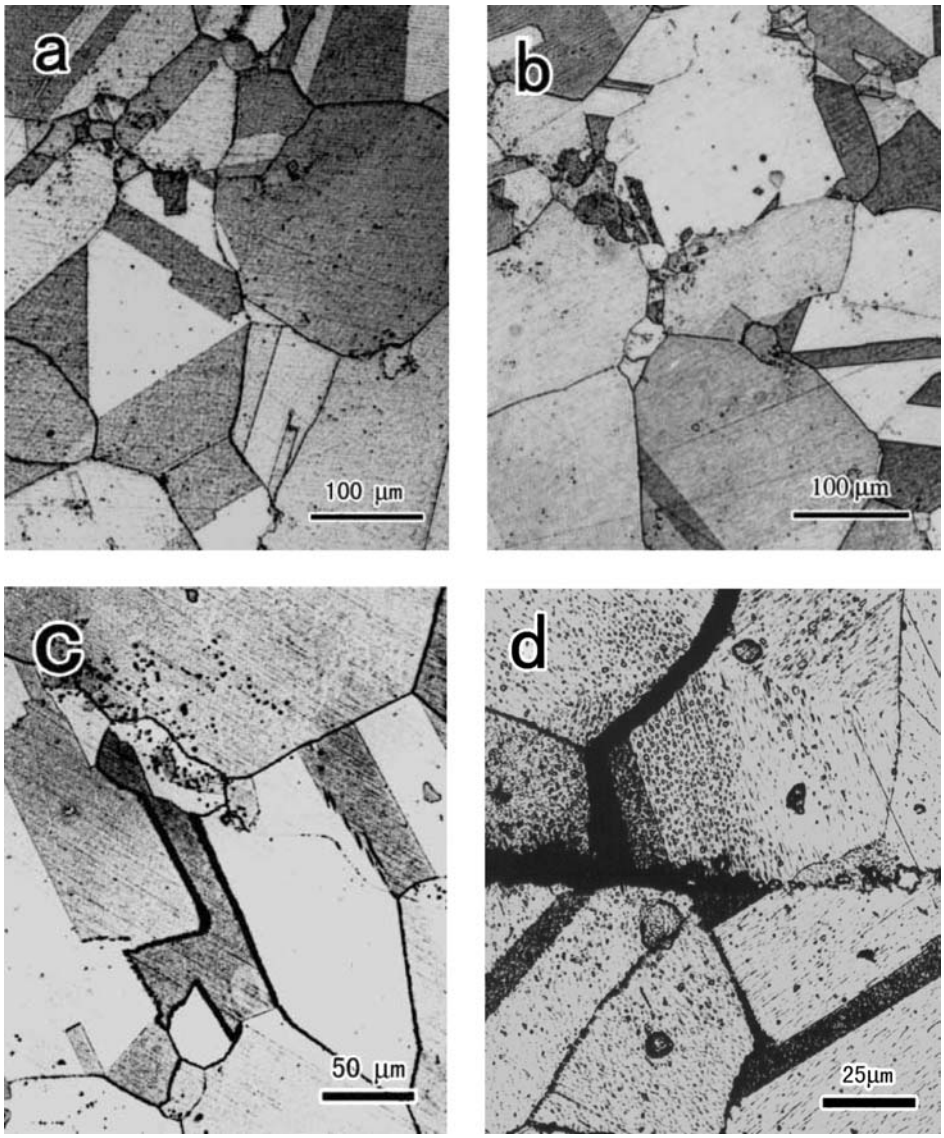

Figure 10 Optical micrographs showing the morphology and the distribution of foreign particles in crept specimens tested at $\sigma = 500$ MPa: (a) $t = 1000$ h; (b) $t = 3500$ h; (c) and (d) creep rupture.

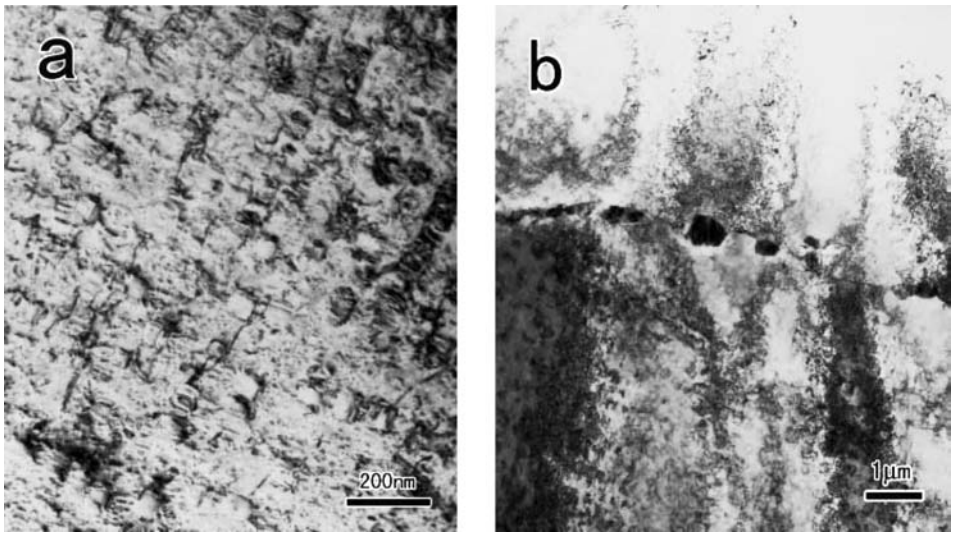

Figure 11 TEM micrograph showing the distribution of dislocations structures in crept specimens tested at $\sigma = 500$ MPa: (a) $t = 3500$ h; (b) creep rupture.

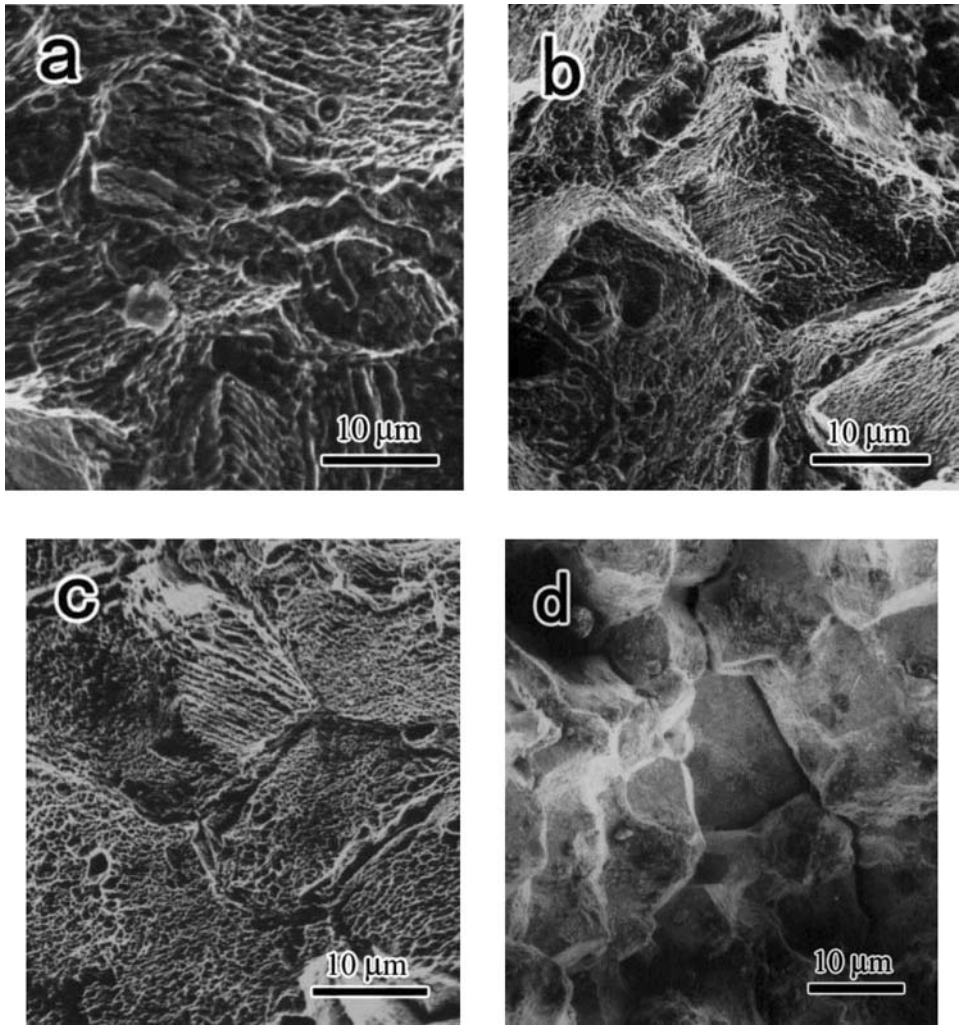

Figure 12 Fractographies of specimens tested at $\sigma = 500$ MPa with different creep deformation: (a) $t = 10$ h; (b) $t = 2000$ h; (c) $t = 3500$ h; (d) creep rupture.

(c) With increasing number of pre-straining cycles, the tensioned fracture of the cyclically deformed specimens presents the transition features from ductile to brittle mode, which well accords with the reduction characterization of the ductile properties or the static toughness during fatigue failure process of the alloy.

2. The investigation regarding the effect of and creep loading on the tensile mechanical properties of the present superalloy at an elevated temperature leads to the following conclusions.

(a) Under creep loading, the strength parameters ($\sigma_{0.2}$ and σ_b) tend to increase, as a whole, while the ductile parameters (δ and φ_f) and the static toughness (U_t) exhibit continuous decrease with increasing creep deformation.

(b) OM examinations show that, as the amount of creep deformation increases, both the morphology and the distribution of foreign particles in the alloy undergo an insignificant variation, as a whole. TEM observations indicate that, under creep loading, the principle deformation mode for the present superalloy was particle cutting rather than dislocation bowing. The formation of boundary cavities in crept specimens is mostly associated with carbide particles as well as vacancies and micro-voids.

(c) With the increase of creep deformation, the tension facture surface exhibits a transition feature from a ductile transgranular fracture to a low ductile intergranular rupture, which is in accordance with the reduction characteristics of the ductile properties or the static toughness during creep failure process of the alloy.

References

1. H. E. BOYER, in "Atlas of Stress-Strain Curves"(Metals Park. Ohio44073, ASM INTERNATIONAL, 1987) p.1.
2. B. WILSHIRE and D. R. J. OWEN, in "Creep and Fracture of Engineering Materials and Structures" (West Cross, Swansea, 1981) p. 447.
3. D. BOBROW, A. ARBEL and D. ELIEZER, *J. Mater. Sci.* **26** (1991) 2045.
4. D. Y. YE and Z. L. WANG, *Mater. Sci. Eng.* **A297** (2001) 54.
5. P. K. LIAW, A. SAXENA and J. SCHAEFER, *Eng. Fract. Mech.* **32** (1989) 675.
6. T. AKAHORI, M. NINOMI and K. FUKUNAGA, *Metall. Mater. Trans.* **A31** (2000) 1937.
7. Southeastern Electric Power Test & Research Institute. Acceptance Tests on High-Temperature Nickel based alloy GH4145/SQ. SEPTRI 09-124 (1995) (in Chinese).
8. Y. H. ZHAO, *China Electricity* **32** (1999) 18.
9. A. L. BRADLEY and N. JAYARAMAN, *Mater. Sci. Eng.* **66** (1984) 151.
10. D. Y. YE, D. H. PING, Z. L. WANG, H. H. XU, X. Y. MEI, C. W. XU and X. L. CHEN, *ibid.* **A373** (2004) 54.

11. M. VALSAN, P. PARAMESWARAN and K. BHANU, *Metall. Trans.* **A23** (1992) 1751.
12. S. GANESH SUNDARA RAMAN and K. A. PADMANABHAN, *Fatigue* **16** (1994) 209.
13. B. LERCH and V. GEROLD, *Acta Metal* **33** (1985) 1709.
14. B. LERCH and V. GEROLD, *Metall. Trans.* **A18** (1987) 2135.
15. R. E. STOLTZ and A. G. PINEU, *Mater. Sci. Eng.* **34** (1978) 275.
16. R. W. HAYES AND P. L. MARTIN, *Acta Metal* **43** (1995) 2761.
17. R. B. GIRDWOOD and R. W. EVANS, *Int. J. Pres. Ves. Piping* **66** (1996) 141.

Received 28 December 2004
and accepted 18 April 2005